



Mineralogical and Elemental Trends in Regolith on Historically Managed Sites in the southeastern United States Piedmont

Paul A. Schroeder · Jason C. Austin · Aaron Thompson · Daniel D. Richter

Accepted: 5 September 2022 / Published online: 4 October 2022
© The Author(s), under exclusive licence to The Clay Minerals Society 2022

Abstract The deep regolith of the southeastern United States has undergone rapid erosion in the last two centuries due to intensive agricultural practices, which has altered the landscape and its inherent fertility. Parent material, landscape position, and land use are important factors in controlling the mineral and elemental composition of soil profiles. Independent quantitative X-ray diffraction (QXRD) and whole-rock chemical analysis of eight weathering profiles agreed well and allow mineral reaction pathways to be constrained as particles are conveyed in the subsurface. QXRD analysis of saprolite, argillic, and soil A-horizons in the profiles highlights the imprint of bedrock on the regolith, which includes Neoproterozoic metatonalitic to meta-granodioritic and Paleozoic meta-granitic to biotite- and amphibolite-gneissic lithologies. Also, aeolian input slightly influenced A-horizon composition. The clay mineral assemblage is dominated by kaolinite, but profiles differ in the amount of interstratified clay minerals, halloysite, hematite, goethite, and gibbsite. Rare-earth element totals vary between 30 and 1048 ppm and

are generally correlated positively with clay and clay mineral content. Eu and Ce anomalies reflect parent rocks and subsequent hydrolysis and redox history, with trends depending upon landscape position and clay content in the weathering profile. Weathering profiles on a high-order interfluvium and those that were actively cultivated have thick argillic horizons (as defined by clay mineral abundance) and are depleted in alkali and alkaline-earth elements. Profiles proximally developed on old-field pine and never-cultivated hardwood forest land do not show large differences in mineral composition trends, whereas profiles on old-field sites with ongoing cultivation exhibit assemblages enriched in clay minerals and (oxyhydr)oxides. Old-field pine sites that were historically eroded by previous cultivation tend to have shallower and thinner argillic horizons, which may well impact critical-zone processes involving gas and water fluxes. This study highlights that mineral compositions of deep regolith, saprolite, and shallow soil horizons are dependent on local geomorphology (i.e. watershed- and hillslope-orders). Quantifying soil and regolith compositional trends across the landscape is a prerequisite for determining rates of chemical and physical erosion on human and geologic time scales.

P. A. Schroeder (✉) · J. C. Austin
University of Georgia, Department of Geology, Athens, GA
30602-2501, USA
e-mail: schroe@uga.edu

J. C. Austin · D. D. Richter
Duke University, Earth and Climate Sciences Division, Nicholas
School of the Environment, Durham, NC 27708-0328, USA

A. Thompson
University of Georgia, Department of Crop and Soil Sciences,
Athens, GA 30602, USA

Keywords Quantitative X-ray diffraction · Rare earth elements · Regolith · Ultisol · Weathering

Introduction

Over a decade of critical zone research demonstrates that landscape evolution is controlled by disparate

processes ranging from tectonic forces to solar energy inputs and biologic activity, including human activity (Banwart et al., 2012; Brantley et al., 2017; Lebedeva and Brantley, 2013; Wymore et al., 2017). Variability of mineral and element content in the regolith can influence attributes such as soil tilth and fertility, hydrologic storage and fluxes, and gas fluxes and composition; all of which are important for sustaining human activities (Richter et al., 2020). Regolith variability can also influence the recording and preservation of paleoclimate signals in paleosols and exogenic carbon, nitrogen, and oxygen cycling; all of which are key to understanding geologic systems over millennial to million-year timescales (Berner, 2004; Cecil, 2003). Critical zone science now offers a multidisciplinary approach to explore the chemical and mineral composition of the regolith in the context of biologic, hydrologic, atmospheric, and anthropogenic dynamics. Soil A- and B-horizon mineral and element contents may be influenced by: 1) plant nutrient uptake and recycling, 2) historic erosion rates, 3) hydrolysis and redox reactions with soil water, 4) chelation and microbial activity, 5) leaching, 6) adsorption of contaminants to clay minerals and (oxyhydr)oxides, 7) precipitation of natural nanophases, 8) aeolian input, and 9) historic amendments.

The purpose of this paper was to provide a quantitative understanding of the mineralogical and chemical character of proximally located regoliths formed on intensely eroded landscape over geologic and historic time. The subsurface profiles in this study were formed under contrasting influences of land use history, interfluvial- and hillsloped-order location (Brecheisen et al., 2021), and underlying geologic parent material. A first challenge was reconciling independent quantitative measures of soil composition, because of the numerous phases with variable crystal chemistry, including disordered phases such as nanocrystalline (oxyhydr)oxides and interstratified (i.e. mixed-layered) clays (Raven and Self, 2017). Such quantitative assessments are key to reactive transport models (Li et al., 2017) and essential for any aspiration to forecast or hindcast the dynamics of the critical zone on both short and long timescales (Sullivan et al., 2020). Therefore, a goal of this study was to compare and contrast the abundances of minerals and chemical elements, to better inter-relate biologic, hydrologic, atmospheric, and anthropogenic metrics within the architecture of the critical zone. The hypothesis tested was that the saprolites in deeply weathered regolith inherited many key mineral and elemental properties from parent rocks

that were subsequently passed into the upper soil horizons, where they influenced above-ground productivity and land-use capacity. A further hypothesis was that the mineralogical and elemental composition of the upper soil horizons is influenced by landscape management, the history of aeolian processes, and landscape position and evolution.

Study Sites and Methods

The study site is ~15 km southwest of Union, South Carolina in the Southern Piedmont of the United States on the Calhoun Critical Zone Observatory (CCZO), one of nine sites supported by the U.S. National Science Foundation (NSF) (Fig. 1). This region is characterized by gently rolling hills on saprolitic Ultisols with regoliths up to 40 m deep (Bacon, 2014; Bacon et al., 2012; Holbrook et al., 2019). The fluvial drainage in this region developed in dendritic patterns that are associated with a range of interfluvial orders and “hillslopes” (Brecheisen et al., 2019a, 2021), with each interfluvial order having experienced a wide range of land uses dating back to Native American habitation. Many areas experienced severe land degradation and accelerated erosion since European colonization (Coughlan et al., 2017, Coughlan & Nelson, 2018). Interfluvial orders of the highest orders (≥ 3) are the most deeply weathered, in contrast to lower order (≤ 3) interfluvial orders and their stream channels, which occasionally reveal bedrock (Jordan, 2020). Depth to bedrock appears to “mirror” the respective topography (St. Clair et al., 2019). In other words, the transport-limited, eroded, high-order interfluvial orders have thicker regolith than the thin regolith found in chemical weathering-limited eroded stream channel environments.

At four research watersheds within the CCZO, eleven profiles were selected for detailed study, based largely on differences in geomorphology and land-use history (Table 1). The sites were thus selected to provide information on the controls of lithology, geomorphology, and land-use history. The old-field pines have grown from previously cultivated fields approximately 70 to 90 years ago (i.e. pines established from the 1930s to 1950s).

Geologic mapping has placed parts of the CCZO in the Neoproterozoic to Cambrian Cat Square terrane consisting of meta-granite units containing biotite and phengite, which suggests an S-type granite with a supracrustal source (i.e. partial melting of ocean

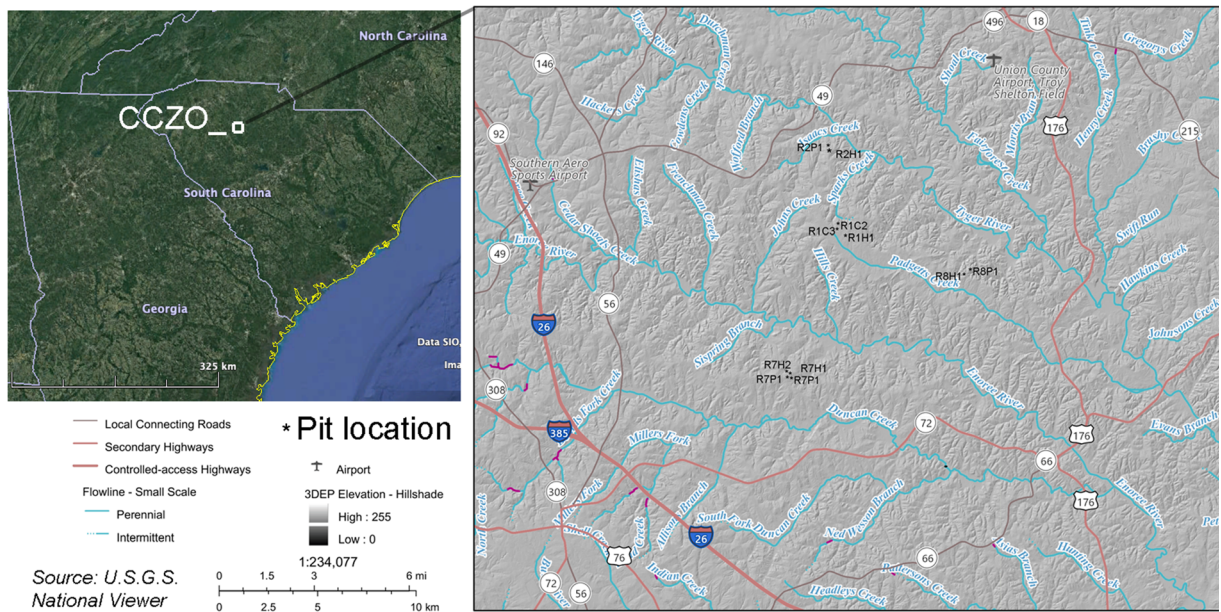


Fig. 1 Location map of the study area. Upper left is a regional map with the location of the Calhoun Critical Zone observatory (CCZO). Larger lower right is a hillshade map of the CCZO (nationalmap.gov) to exemplify dendritic geomorphic landscape, major rivers (flowing from NW to SE), and broad, high-order

interfluvial areas (typical of the S.E. U.S. Piedmont). Pit locations are clustered at the given scale and indicated by small black stars. GPS coordinates for each site are available in Table 1. See also Cook (2019) for photographs of the pits

sediments) (Huebner et al., 1977; Jordan, 2020). Other parts of the CCZO can be associated with the Charlotte terrane occurring with biotite-hornblende-quartz meta-diorite and meta-tonalite, which can be most closely linked with the Wildcat Branch Complex mapped to the west (Dennis & Wright, 1997; Horkowitz, 1984). The lithologic contrast between these felsic and

intermediate bodies implies fault boundaries. Although not clear in the field, they were most likely manifested as overthrusts placed unconformably on the westernmost extent of the CCZO and a suture defining window (i.e. fenster) to the east in this nappe tectonic regime. The placement of the CCZO in the broader regional geologic mapping context of the Whitmire reentrant

Table 1 General characteristics of the profiles under study

| Research Area and profile code | Land-cover | Interfluvial order (hillshaded order) [^] | Average slope and aspect | Latitude | Longitude | Severity of historical erosion | Surface elevation (m) |
|--------------------------------|-----------------|--|--------------------------|----------|-----------|--------------------------------|-----------------------|
| R1H1 | Hardwood | 3 | 2% E | 34.6065 | -81.7336 | Minimal | 181.0 |
| R1C2 | Cultivated crop | 3 | 0 % | 34.6114 | -81.7279 | Severe | 184.6 |
| R1C3 | Cultivated crop | 3 | 3% SW | 34.6092 | -81.7280 | Severe | 177.9 |
| R2H1 | Hardwood | 2 | 15% NE | 34.6475 | -81.7329 | Minimal | 149.1 |
| R2P1 | Old-field pine | 2 | 7% N | 34.6452 | -81.7327 | Moderate | 164.1 |
| R7H1 | Hardwood | 2 | 6% NW | 34.5420 | -81.7549 | Minimal | 164.6 |
| R7H2 | Hardwood | 2 | 7% NNW | 34.5424 | -81.7557 | Minimal | 160.9 |
| R7P1 | Old-field pine | 2 | 5% N | 34.5414 | -81.7553 | Minimal | 166.6 |
| R7P2 | Old-field pine | 2 | 8% SE | 34.5412 | -81.7541 | Severe | 162.7 |
| R8H1 | Hardwood | 2 | 5% N | 34.5887 | -81.6576 | Minimal | 166.3 |
| R8P1 | Old-field pine | 2 | 11% SE | 34.5907 | -81.6542 | Severe | 159.8 |

[^]Brecheisen et al. (2021)

(an arcuate belt that is concave toward the foreland and behind the main thrust front) emphasizes the complex fold and fault relations that exist in the CCZO subsurface. The bedrock may change composition in both vertical and horizontal directions on a scale of tens of meters. Unaltered bedrock was sampled from below only one regolith profile in this study, but elemental and thin section analyses of nearby outcrops by Jordan (2020) are consistent with regional geology. In the present study, most regolith was sampled to ~8 m depth, so it might reasonably be inferred to be the parent material from the deepest saprolite sampled. Over regolith thicknesses of 8 m, heterogeneity of parent material in each profile is possible. In some cases, foliations were obvious, as seen in the photographs of the 2–3 m deep sections of the profiles studied by Cook (2019).

Each site was excavated with a backhoe to form pits ~3 m wide by 3 m deep. Auguring was used to retrieve deeper samples down to 8 m below the surface, unless hand auger refusal was met. Sample locations and depth intervals were recorded and registered according to the System for Earth Sample Registration (SESAR) and assigned an International Geo Sample Number (IGSN) and listed in Table S1 using a local labeling scheme that identifies research watershed (R), cover type (where C = cultivated, P = pine, H = hardwood), and pit number. Ancillary biological and physical data (formal soil descriptions, density, color, root density, climate, land use, LIDAR, stable isotopes, soil gas, moisture, texture, and vegetation) and photographs of the pits were archived with the NSF-CZO repository (<https://www.hydroshare.org/group/148>). Samples were archived at Duke University with various splits distributed among CCZO scientists. Approximately 5-g splits were sent to Activation Laboratories Ltd. in Ancaster, Ontario, Canada for elemental analysis. Samples were ground using 4Litho® protocols, which employs lithium metaborate/tetraborate fusion of powdered samples into a molten bead and that were digested in dilute nitric acid solution. Analysis of the solution was by inductively coupled plasma (ICP) optical emission spectroscopy (-OES) and ICP mass spectrometry (-MS). Detection limits were 0.01% for major oxides, 0.001% for minor oxides, and for trace elements ranged from 30 to 0.04 ppm (see Table S1). Typical values of duplicates ranged within $\pm 2\%$ of the reported average value. All analyses were quality controlled with 12 certified external samples analyzed concurrently with differences typically $<0.5\%$ between measured and certified values.

Rare earth element and yttrium (REY) distributions were evaluated by first normalizing the elemental abundances to average values for C1 chondrites (Anders & Grevesse, 1989) and then either plotting the normalized abundances or by using abundance ratios. These ratios are: (1) the Ce anomaly, $Ce/Ce^* = 3Ce/(2La+Nd)$ (Braun et al., 1990); (2) the Eu anomaly, $Eu/Eu^* = 2Eu/(Sm+Gd)$ (Vázquez-Ortega et al., 2015); and (3) Y/Ho (Bau, 1999), where Y, La, Ce, Nd, Sm, Eu, Gd, and Ho correspond to the chondrite-normalized REY concentrations. Ce/Ce^* and Eu/Eu^* values higher or lower than unity represent enrichment or depletion relative to the chondritic ratios. These metrics were chosen with an underlying hypothesis that the redox-sensitive nature of Ce and Eu will produce different weathering profiles and across landscapes. Y and Ho are not redox sensitive, but Y/Ho values represent departures relative to the chondritic ratios.

Samples for quantitative X-ray diffractometry (QXRD) were oven dried at 60°C and crushed by mortar and pestle to entirely pass a 125 μm sieve. Powders were mixed with a zincite (ZnO) internal standard and carefully weighed at a ratio of 10:1. The mixtures were ground for 10 min with ethyl alcohol in a McCrone® micronizing mill with corundum grinding pucks. Slurries were dried at 60°C and the powder was back-filled and pressed (Hurst et al., 1997). QXRD data were collected using a Bruker D8 Advance® diffractometer (Madison, Wisconsin, USA) employing Co-radiation, a $FeK\beta$ -filter, and a Lynx-Eye detector, with scan parameters: range = $2-80^\circ 2\theta$, step = $0.01^\circ 2\theta$, rate = 0.1 s per step. Bruker EVA® software was used to correct for sample displacement error and strip the $K\alpha_2$ signal. Mineral identification was accomplished using EVA and the International Centre for Diffraction Data powder diffraction file – PDF4+ 2020. Structure files for best-fit phases were exported from the PDF4+ database and used as input for Rietveld refinement (Rietveld, 1967) with the Bruker Topas® software. Allowing for minimization of structural factors including lattice parameters, intensity, coherent scattering domain size, and in some cases, preferred orientation bias, final model results were achieved with weighted profile residuals (R_{wp}) ranging from 9 to 14%. Model results with higher R_{wp} values were typical of samples with abundant interstratified clays (e.g. hydrobiotite) for which structural models are not available. Two kaolinite structure models were employed to improve the fitting process. In effect, one kaolinite model structure used a high-defect density

parameter constraint (i.e. small coherent scattering domain size) and the other used a low-defect density parameter constraint. Variations in the $\sim 7 \text{ \AA}$ $00l^*$ c dimension were also used to simulate small amounts of what was assumed to be interstratification of micas and/or halloysite. Note that the Topas® algorithm does not accommodate interstratified structures such as hydrobiotite and randomly ordered layer combinations. Advances to accommodate such structural disorder in the Rietveld method have been developed by Dietel et al. (2019) and Ufer et al. (2004, 2008). Misfits between model and observed data are inherent in this current study and are addressed in the Results and Discussion section below.

Selected samples were size separated to the $<2 \mu\text{m}$ equivalent spherical diameter fraction using standard methods (Moore & Reynolds, 1997; Schroeder 2018). Slurries were deposited on glass slides and dried to produce an oriented clay layer, which was scanned from 2 to $40^\circ 2\theta$ in the air dried; ethylene glycol-saturated; formamide-saturated; and 110°C -, 350°C -, and 550°C -heated states. Multiple cation saturation methods and a discussion of the interstratified clay minerals in the fine fraction from two of the pits were presented by Austin et al. (2020) in the context of land use and hillslope position.

To evaluate precision and accuracy of QXRD, the mass fraction of a known zincite internal standard was determined for each sample by independent minimization of the scaling factor in the Rietveld refinement. A plot of known internal standard concentration versus instrumentally determined internal standard concentration for all samples ($n = 117$) revealed an average difference of $-0.8 \text{ wt.}\%$ (i.e. smaller than the known values), with a standard deviation of $1.4\% \text{ wt.}\%$ (Table S2).

Using mineral abundances and mineral stoichiometry, calculation of the bulk chemical composition of each sample was possible. Major oxide totals were calculated using assumed mineral stoichiometries. Regionally representative minerals that exhibited solid solutions (i.e. feldspars and micas) or changes associated with weathering (e.g. degraded micas) were independently analyzed by energy dispersive spectroscopy (EDS) using polished epoxy grain mounts with reference minerals for calibration (Cannida, 2018; Sanders, 2018; Schroeder et al., 2020; Fig. S26). EDS was performed using a JOEL 8600 microprobe (Peabody, MA, USA) and a Thermo Fisher Teneo field emission

scanning electron microscope [A1] [A2] (Waltham, MA, USA), both fitted with Oxford EDS detectors (Concord, MA, USA) and located at the University of Georgia. Model stoichiometries for each mineral used in the recalculation are presented in Table S1.

The soil pits and cores to 8 m did not reach unweathered parent material. Several hard rock samples were collected from within the CCZO as part of a geologic mapping effort (Jordan, 2020) and an earlier study of a deeply drilled core to 65 m (Bacon et al., 2012). These rocks were generally described as granitic gneiss and amphibolitic gneiss. Chemical and mineral analyses were performed using the same methods on selected samples from Jordan (2020) with results presented in Table S1. Chemical analysis was also performed on a subset of seven samples from the deep coring study (Bacon et al., 2012; Holbrook et al., 2019) from the surface to a depth of 12.4 m. The deep core site (R1H1) is within a hardwood forest with a slope of $<2\%$, at an elevation of 181 m on the highest-order interfluvium in the CCZO (Brecheisen et al., 2021). Photographs of thin sections of mounted grains from samples from the weathering profile of the R1H1 site are presented in the Supplementary Materials (Fig. S27) with the aim of illustrating the typical particle sizes and minerals that can be resolved optically.

Results

All quantitative mineralogical and chemical data are contained in Table S1 and discussed in more detail in the Supplementary Materials. Plots of major oxide abundances as measured by chemical methods versus the major oxide abundances predicted from mineral abundances and stoichiometry were compared to evaluate analytical accuracy. Figure 2 shows $\text{wt.}\%$ major oxide cross plots of all samples with solid lines depicting a 1:1 slope and dashed lines showing least-square linear regressions. SiO_2 values ranged from ~ 50 to 90% and a best-fit line with $r^2 = 0.73$ (Fig. 2a). Assuming chemical data are independent variables ($n = 117$), the trend line and standard error (SE) indicate that QXRD overestimated SiO_2 with an uncertainty of 4.7% . Al_2O_3 QXRD values ranged from ~ 7 to 35% and a best-fit line with $r^2 = 0.61$ (Fig. 2b). The trend line and SE indicate that QXRD under-measured Al_2O_3 with an uncertainty of 3.3% . QXRD Fe_2O_3 total values ranged from ~ 0 to 12% and a best-fit line with $r^2 = 0.60$ (Fig. 2c). The trend

line and *SE* indicate that QXRD under-measures Fe_2O_3 with an uncertainty of 3.3%. K_2O values ranged from ~0 to 7% and a best-fit line with $r^2 = 0.79$ (Fig. 2d). The trend line and *SE* indicate that QXRD over-measured K_2O by 0.79%. Loss on ignition (LOI) reflects volatile components that are mostly water from hydroxyl groups in the samples studied (gain on ignition due to oxidation of ferrous iron was assumed to be negligible). A plot of LOI versus H_2O indicated a range of LOI values from 1 to 12% and H_2O from 2 to 14% and a best-fit line with $r^2 = 0.74$ (Fig. 2e). If LOI is considered equal to H_2O , then the trend line and *SE* indicate that QXRD under-measured H_2O with an uncertainty of 1.4%. Na_2O values ranged from about 0 to 4% and a best-fit line with $r^2 = 0.93$ (Fig. 2f). The trend line and *SE* indicate that QXRD under-measured Na_2O with an uncertainty of 0.3%. All other elements appeared with such low concentrations that QXRD was not sensitive enough to measure trace minerals and not enough trace element information was available to include in the major mineral stoichiometry. Specific trace REY trends will be considered below in the analysis of individual profiles.

In summary, QXRD slightly over-estimated SiO_2 , Al_2O_3 , and K_2O and slightly under-estimated Fe_2O_3 , H_2O , and Na_2O . These differences are assigned to: (1) slight systematic miscalibration in the Rietveld method, (2) inexact stoichiometry assignments for the minerals, (3) the presence of interstratified clay minerals and poorly ordered (oxyhydr)oxide phases that are not accommodated by the Rietveld model, and (4) relatively small errors in the chemical assays. For this study, which was aimed at comparing mineral and chemical trends in related suites of regolith materials, it was assumed that the relative mineral and chemical trends and changes have sufficient fidelity to allow for future assessment of regolith development in the context of mass balancing of weathering reactions as well as of mineral and elemental abundances trends in the context of landscape position and land use.

The extent of regolith alteration is evaluated commonly using τ_j -plots, where the least soluble elements (e.g. $j = \text{TiO}_2$) and minerals (e.g. $j = \text{quartz}$) are employed to determine the extent to which elements or minerals have been depleted or enriched within an often-assumed isovolumetric space of known density (Brimhall & Dietrich, 1987). In the current study, the Hauser et al. (2020) approach was used, in which the deepest regolith sample in each of the profiles was

assumed to have the attributes of the underlying bed rock and thus τ_j can be calculated relative to the deep saprolite. It was also assumed that at 8 m depth the physical rooting influence is minimal (Hauser et al., 2020) and weathering is isovolumetric. This approach accentuates changes that have taken place in an assumed otherwise steady state rate of weathering, where the rate of uplift, downward propagation of the weathering front, and the developed argillic horizon are all in dynamic equilibrium (Hack, 1975). For this reason, Figs S1 to S10 show τ_j values ($j = \text{TiO}_2$) for the major oxides relative to deep regolith of each profile, along with mineral abundances.

Results in the context of each profile and its respective watershed, interfluvial, or hillshed order; landscape position; and land management are presented in the supplementary material. In Figs S1 to S10, metrics useful for assessment of weathering and the nature of regolith development are plotted. Plots relative to each surface for all profiles are: the τ_j plot, QXRD mineral abundances, chondrite-normalized rare earth element trends, and a chemical index for clay mineral and (oxyhydr)oxide content based on the sum of $\text{Al}_2\text{O}_3 + \text{Fe}_2\text{O}_3$ (total) + H_2O (assuming LOI proxies for structural H_2O).

The supplementary material also includes selected results of detailed clay mineralogy studies (Figs S15–S25). In summary, qualitative evidence for halloysite and smectite was observed in the deeper portions of saprolite. Biotite was the dominant mica and phengite was a minor mica in the deep saprolite samples. Commonly, hydrobiotite and other interstratified clays such as kaolinite/biotite and kaolinite/vermiculite appeared in the upper portions of the regolith. These interstratified clays were previously characterized by Austin et al. (2020). Plagioclase feldspars were detected in the deep regolith but were observed rarely in the argillic and A-horizons. Potassium feldspars (K-spars) often persisted throughout the saprolite, generally decreasing in abundance toward the top of the profile. In many instances, K-spars increased in the A-horizon relative to the argillic horizon, which may be partially related to aeolian input as discussed below.

Discussion

The discussion below considers first the saprolites in the pits studied. The bedrock parent material varies from intermediate to felsic composition (Jordan, 2020).

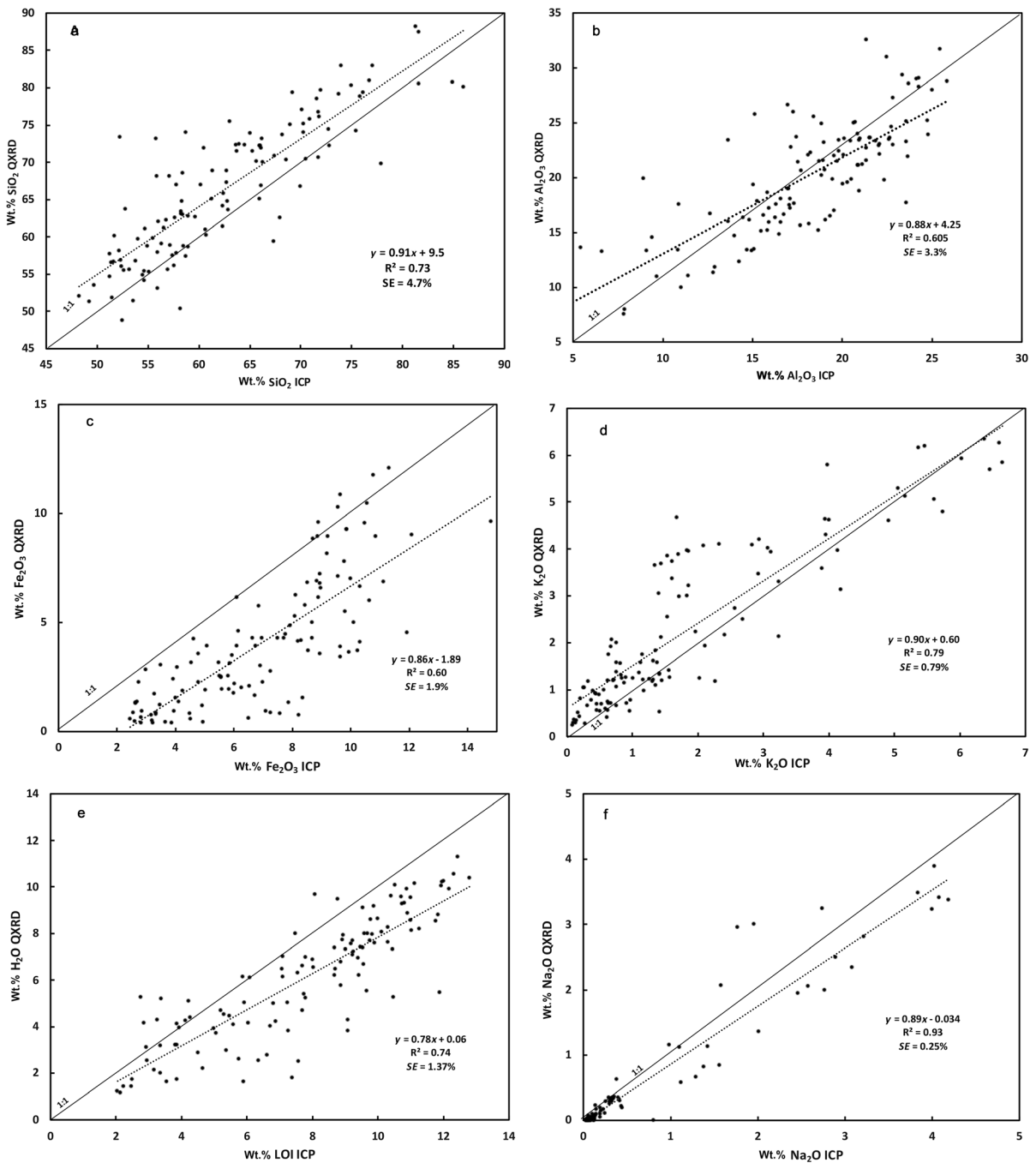


Fig. 2 Weight percent abundance of major oxides as determined by ICP-MS versus abundance of major oxides as determined by QXRD and assumed mineral stoichiometries (see Table S1 for structural formulae). All plots have included 1:1 line (solid line), least square linear ($y = mx + b$) minimization fit (dashed line), slope

and y intercept coefficients, correlation coefficient (R^2) and standard error (SE) **a** SiO₂, **b** Al₂O₃, **c** Fe₂O₃ (total), **d** K₂O, **e** H₂O assuming loss in ignition (LOI) proxies for H₂O, and **f** Na₂O. See text for discussion regarding differences between 1:1 and fit lines

Subsequent overprinting of the saprolite by oxidation and hydrolysis reactions may also have been variable in the context of landscape position and land use.

Secondly, the argillic B-horizons and quartz-rich A-horizons are discussed in the context of landscape position, land use, and potential sources of allochthonous

material (e.g. aeolian input, tilling, creep, tree-throw, and burrowing) that can impact mineralogy and chemical composition. Although particle-size analyses (i.e. sand-silt-clay) were not included in the current paper, the pit soil horizons were described by U.S. Department of Agriculture soil scientists. These horizon designations are plotted in Figs S1–S10, which allows for discernment of argillic horizons, which were also based on clay mineral abundances and the $\Sigma\text{Al-Fe-H-oxides}$ plots observed in this study.

Saprolite Mineralogy and Chemistry

The ability to distinguish different parent rock types is key to comparisons of mineralogical and chemical properties among each pit and to the general understanding of how soil profiles develop. Geophysical evidence (Holbrook et al., 2019; St. Claire et al., 2019) suggests that regolith depth varies widely from 1 to 40 m across the CCZO. Depth to bedrock can vary drastically over a short distance, which makes it difficult to know the exact depth to bedrock immediately adjacent to any coring location. Uncertainty is added by the possible presence of core stones that may appear to be bedrock, while weathering fronts may extend much deeper (see e.g. Schroeder, 2018).

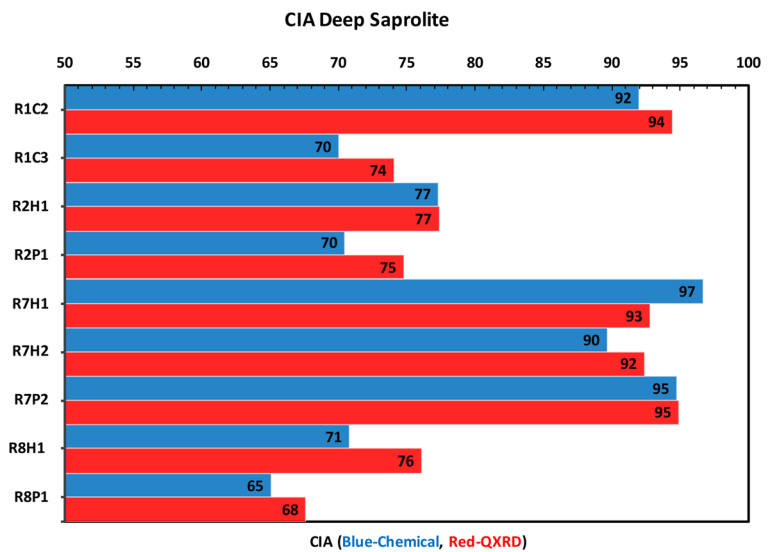
In the current study, the absence of bedrock sampling led to the use of saprolite at 8 m for an assessment of parent material variation. The ability to distinguish different rock types from saprolite using indices of weathering, such as the chemical index of alteration (CIA), was evaluated by Price and Velbel (2003). They studied similar weathering profiles on heterogeneous metamorphic rocks located 160 km west of the CCZO that included the Coweeta Group and Otto Formation in the Blue Ridge Province. Price and Velbel (2003) noted that molar-based CIA values of bedrock averaged about 12 points lower than those of saprolite (i.e. $75_{\text{saprolite}} \longleftrightarrow 63_{\text{bedrock}}$) and in some cases using saprolite to differentiate parent material in their suite of rocks was deemed marginal. The present authors agree that saprolites experience variable degrees of selective dissolution and precipitation, hydrolysis, and redox reactions, which lead to uncertainties in defining parent-rock composition from saprolite. To assess the validity of discerning parent material at the CCZO sites using 8 m deep saprolite (Fig. 3), the respective oxide-based CIA differed slightly from the molar-based CIA values, as defined by Nesbitt and Young (1982). Regardless of

mass or molar basis for CIA values, the same relative trends were manifested. Mass-based CIA values were determined independently by both chemical and QXRD methods at 8 m (except R1C3 at 6.5 m). Deep saprolites fall into two distinct groups: (1) those with “low” CIA values (ranging 65 to 77); and (2) those with “high” CIA values (ranging 90 to 97). Deep saprolites in R1C3 and all R2 and R8 sites exhibited the lower range of CIA values, which indicates lower degrees of weathering. Deep saprolites in R1C2 and in all R7 sites (irrespective of vegetation cover type) exhibited high CIA values, which signals more extensive weathering. Use of saprolites with high CIA values alone for assessing parent material is ambiguous, as suggested by Price and Velbel (2003). Differentiating parent rock types using CIA in pits R1C2 and R7 was, therefore, inconclusive.

Considering the deep saprolites for sites R8 and R2 with low CIA values (<75) may offer insight about parent rock, but cover type and landscape position pose added factors. When R8 and R2 saprolites were paired by cover type, slightly higher CIA values were observed in the hardwood sites (i.e. more weathered) and lower values in the old-field pine sites (i.e. less weathered). This suggests a control by cover type; however, when sites were paired by elevation, where the R8 pine site is higher in elevation than the hardwood ($\Delta 6.5$ m) and in R2 the hardwood is higher in elevation than the pine ($\Delta 15.1$ m), respectively, the landscape elevation and cover type act independently. Landscape elevation differences with similar cover type may explain a lower CIA value, such as observed in the deep saprolite of R1C3, which sits down slope from R1C2 ($\Delta 6.3$ m). The nearby R1H1 site, with a hardwood cover and an elevation close to R1C2, has a CIA value of 78 at 8 m depth, similar to R1C3. The R1 cover type and higher-order interfluvial positions again made direct comparisons of CIA difficult. The present authors agree with Price and Velbel (2003) that the ability to make distinctions about differences in parent material using only CIA of saprolite is marginal; however, high values of CIA do appear to indicate length of time of exposure to weathering. If soil exposure time could be determined by using cosmogenic nuclides, then this would further refine this understanding.

Factors of soil development also must consider historical erosion of lands induced by farming practices, as noted by Ryland et al. (2020) who compared locations at the CCZO with less disturbed nearby reference sites. They considered hillslope position and slope, which

Fig. 3 Chemical alteration index (CIA) for saprolite samples. Independent values derived from ICP-MS (Blue) and QXRD (Red) show reasonable agreement. Saprolites from R1 and R7 group with high values indicating intense weathering, with the exception of R1C3 which is downslope and refused auger at 6.5 m and at a midpoint in the catena. R2 and R8 group with low values indicating less intense weathering



were factors related to the measured depth to the upper layers of the argillic horizon. Their observations are discussed below in the context of argillic horizon mineralogy and chemistry. While the depth to bedrock was also not explored in their study, it is important to note that farming and other anthropogenic factors may influence CIA at depths of 8 m. For example, a post-1900 loss of 1 m of topsoil would put saprolite that was once (i.e. pre-legacy) at 9 m depth now at 8 m depth (today).

Despite the overprinting of different degrees of weathering and erosion as shown by CIA at 8 m depth (today), mineralogical and trace element differences suggest variations in parent material. Mineralogy differences noted in R8 contain microcline as the primary potassium feldspar, whereas other sites contain orthoclase. Deep saprolites for R1 and R8 also have greater abundances of biotite and plagioclase feldspar than R2 and R7.

The sum of chondrite-normalized rare-earth-element (REE, not including Y) abundances in the deep saprolites also group R2 and R8 pits together as having higher abundances (average = 287 ppm) and group R1 and R7 pits with lower concentrations (average = 139 ppm), which would suggest variation in parent materials. REE element concentrations in the context of weathered regolith profiles have been examined by Ferreira et al. (2019) and Li and Zhou (2020). In summary, the common tri-valent (III) state of the REEs is associated with late magmatic and later metasomatic alteration in minerals such as monazite, barnasite, parisite, xenotime,

apatite, rhabdophane, cerianite, epidote, and fluorite. Of all the REE, only Eu and Ce occur in another valence state, Eu(II) and Ce(IV), at Earth-surface temperatures. Reduced Eu(II) substitutes commonly in plagioclase and is more common in mafic rocks formed under low-oxygen fugacity magmatic and high-grade metamorphic conditions. Upon weathering, Eu can be oxidized readily to Eu(III), and because the reduction of Eu(III) requires strong reducing conditions rarely encountered in low pressure-temperature systems (Laveuf & Cornu, 2009), differences in the Eu concentrations are likely indicative of different parent rocks (i.e. lower Eu/Eu* in mafics versus higher Eu/Eu* in felsics). Pits in R2, R1, R8, and R7 exhibit average saprolite Eu/Eu* values (depth range 550–750 cm) in increasing order of 0.708, 0.745, 0.793, and 0.876, respectively. This is consistent with R1, R2, and R8 saprolites coming from a more intermediate parent rock type (i.e. plagioclase-bearing) and being less oxidized, whereas R7 saprolite was derived from more felsic rock and is more highly oxidized.

Ce anomalies are not indicative of distinguishing mafic versus felsic parent rock minerals because its oxidation state does not vary under magmatic and metasomatic conditions. In contrast to Eu/Eu*, Ce/Ce* modifications occur as Ce³⁺ oxidizes to Ce⁴⁺ during weathering; enrichment is associated with enhanced adsorption of tetravalent Ce to Mn and Fe oxides (Bau et al., 1996) and clay minerals and enhanced precipitation as an oxide (Braun et al., 1990) relative

to trivalent Ce (further discussed below). Ce anomalies for saprolites from pits in R1 and R7 were more variable than their correlative Eu anomalies, which supports the notion that R1 and R7 saprolites have inherited aspects of their parent rocks and also experienced deeper weathering than R2 and R8. A plot of Ce/Ce* versus Eu/Eu* saprolite values shows the pits grouping by Eu anomalies and spreading by Ce anomalies in R1 and R7 (data in Table S1).

Chondrite-normalized values for three unaltered granitic rocks from within the CCZO studied by Jordan (2020) show much lower REE abundances, with affinities given to rocks from the Cat Square terrain. Jordan (2020) suggests the REE patterns of the CCZO granites have similarities to the Cat Square terrain, which further suggests that the R7 pits have parent rock sources from that terrain, while R1, R2, and R8 may have affinities toward a Charlotte terrain granite. The paucity of geochemical data from the nearby Charlotte terrain precludes any firm assignments, however, except to recognize that parent material within the CCZO is somewhat variable and contains elements of both Neoproterozoic meta-tonalitic to meta-granodioritic and Paleozoic meta-granitic to biotite/amphibolitic gneissic lithologies. The regolith and granite of the younger Liberty Hill pluton to the northwest (Hercynian: ~305 Ma; ~85 km east of the CCZO) have total REE+Y values ranging from 100 to 750 ppm with the granite values being lower than the regolith values (Bern et al., 2017).

Argillic- and A-Horizon Mineralogy and Chemistry

Argillic horizons were assessed (and are defined herein) by the abundance of clay minerals (composed of mostly kaolinite with lesser amounts of interstratified clays, HIV, and smectite) measured by QXRD and by the $\Sigma\text{Al-Fe-H-oxides}$. Differences in soil texture (i.e. % clay by weight) and aggregation (i.e. the degree of soil blockiness and ped formation) were not used in this study, although it is recognized that aggregate development is important to physical and hydrologic properties of regolith (Richter et al., 2020). Depth trend comparisons of clay mineral abundance and $\Sigma\text{Al-Fe-H-oxides}$ for all pits showed good correspondence between the two metrics. By looking at both metrics, argillic horizons (as defined herein by clay mineral abundances) vary considerably in thickness and depth. The R2 and

R8 sites exhibit lower abundances of clay minerals and have thinner argillic horizons. Pits in R1 and R7 have deeper (up to 7 m) and thicker clay mineral-enriched horizons. The R1C2 and R1C3 sites have historically been tilled (and still are) such that an A_p horizon is a clear pedologic feature in both pits.

Invariably, all sites have a greater amount of quartz in the A-horizon than in the argillic horizon. This can be attributed partially to the lower solubility of quartz relative to all other major primary silicate minerals, where the intense weathering promoted by the carbonic and organic acids in the O-horizon selectively hydrolyzed the latter. Also, the translocation of clays (i.e. lessivage) from the A-horizon resulted in a net downward movement of fine material (Calabrese et al., 2018). The absence of orthoclase in the argillic horizons for many of the pits and the presence of orthoclase in A-horizon is most parsimoniously explained as involving an allochthonous source. The assumption that primary minerals in the A- and upper argillic-horizons were being sourced only from below is untenable. As proposed by Schroeder et al. (1997), who observed a similar trend in a granitic Piedmont weathering profile in Georgia, the orthoclase was likely brought in from above by aeolian transport. The source of such allochthonous material has been regionally attributed to westerly aeolian transport of soils active during the glacial climates, most recently between 15 ka and 5 ka but also further back into the Pleistocene (Markewich & Markewich, 1994) when well documented now-stabilized dune fields were formed on the eastern flanks of rivers to the south. If bioturbation, comminution, and creep of the top meter occurred from human cultivation over the past 100 years and natural tree-throw and soil fauna over the past 1000s of years, then the mineral assemblages in the top of the argillic horizons and A-horizon likely experienced mixing. Evidence for this process is supported by stable $\delta^{13}\text{C}$ and $\delta^{18}\text{O}$ isotope signatures in pedogenic gibbsite in an Ultisol located in the Georgia Piedmont (Austin & Schroeder, 2014).

Tau plots (Figs. S1–S10), made assuming the deep saprolite as a reference material is feeding into the upper horizons (in a Eulerian sense), further reveal differences among the various argillic horizons. All sites exhibit argillic horizons that are highly depleted in alkali and alkaline-earth cations. R8 sites and R1C3 exhibit noticeable increases in H_2O (i.e. mostly as hydroxyls in kaolin-group minerals and to a lesser extent gibbsite and goethite). Argillic horizons of

the cultivated sites (RC1) are nearly completely depleted of potassium, even though the two pits can be assumed to have very similar protoliths.

Regarding relative differences between hardwoods and the pines, argillic horizons have variable potassium tau values in comparing the R2 and R7 sites. Tau is >0 for the K_2O cases of R2H1, R7H1, and R7P2, which is consistent with the tree-nutrient uplift theory of Jobbagy and Jackson (2004). Argillic horizons of R8 sites are in part influenced by the more intermediate parent rock below, which has biotite that altered first into hydrobiotite (quantitatively modeled as HIV) (Figs S9, S10). Differences in topographic roughness between R8H1 and R8P1 suggest that the pine site was eroded severely in legacy times (Brecheisen et al., 2021), which was also noted for nearby sites by Ryland et al. (2020). If one assumes that 1 m of the R8P1 site was removed in the past 100 years by accelerated agricultural activity, then that would have brought less weathered saprolite closer to the surface. This is evidenced by a lower abundance of gibbsite, goethite, and kaolinite and $\Sigma Al-Fe-H$ -oxides in the R8P1 site argillic horizon versus the R8H1 site. This is further supported by the occurrence of smectite in the saprolite of the R8P1 site, which the present authors hypothesize would be present at depths beyond 8 m in the R8H saprolite. Brecheisen et al. (2019b) conducted measurements of soil gases and moisture in the same area and similarly suggested that erosion and land use changes to argillic horizons may well impact critical zone processes. The differences in primary and secondary minerals seen deep in R8P1 versus R8H1 profiles (e.g. absence of gibbsite in R8P1) is evidence of different long term pedogenic processes acting at these two sites, which may in part be due to parent material, slope, and aspect (Table 1).

Realizing that the REE measures in the current study are bulk measures in the profiles and do not partition extractable versus bound forms, the trends presented here are mostly to add to the global inventory of REE concentrations in soils. REE trends must be considered in the context of land use. For example, Hu et al. (2006) noted that phosphate fertilizers contain on average 61 ppm Ce and the application of REE supplements is practiced in regions around the world. Richter and Markewitz (2001) detailed a chemical study of many old field pines in the Calhoun Forest, and observed excess extractable Ca and P, which is a signature of historical cultivation. The present authors posit, however, that the inputs were modest

and, thus, minimally contributed to the addition of Ce. The only evidence for soil amendment in the present study was the identification of trace amounts of dolomite in the A-horizon of the R1C pits, so phosphate fertilization did not factor into the REE trends shown. REE trends in the argillic horizon similarly separate pits in R2 and R8 from R1 and R7, where the sum of REE values are larger and smaller, respectively. Li and Zhou (2020) examined extractable total REE in Chinese soils of similar mineralogy and observed the trend of low values in the A-horizon and upper argillic horizon, maximum values in the lower argillic horizon and upper saprolite, and low values again in the lower saprolite. This trend is similar to the R2 and R8. Li and Zhou (2020) attributed this to clay mineral transformation of REE-bearing halloysite to kaolinite, which was also displayed here in R8 using the formamide test (Fig. S25) (Churchman, 1990). The present authors suggest that adsorption of REEs is also possible on the interstratified structures with degraded mica-, vermiculite-, and smectite-layer types.

A key repeating feature of the REE+Y data in the current datasets is the increases in positive Ce anomalies and low Y/Ho ratios (below unity) coinciding with the argillic horizons (Figs S1–S10). Positive Ce anomalies are well known from marine systems, where Ce enrichment associated with the oxidation to Ce(IV) occurs on Fe and Mn oxide-bearing crusts (Bau et al., 1996), and Ce anomalies are used commonly to study weathering intensity (Braun et al., 1990; Hu et al., 2006; Laveuf & Cornu, 2009; Moravec et al., 2021). Ce anomalies in the profiles from this study, in nearly all cases, are positively correlated with clay abundance, which is particularly rich in Fe phases and Fe coatings (Chen et al., 2019). The present authors recognize that some of the reported values are near the detection limits for Ho and Y (0.1 and 2.0 ppm, respectively), which sheds some uncertainty. However, in most profiles a similar deviation of Y/Ho ratios is observed, but not in all. Y and Ho are regarded as geochemical twins and present at their chondritic ratio in nearly all parent rocks, but Ho has a much stronger affinity for Fe oxide surfaces (Bau, 1999) and this leads to low Y/Ho ratios in soil horizons weathering in the presence of Fe phases (Thompson et al., 2013).

A plot of $(Eu/Eu^*)/(Ce/Ce^*)$ versus elevation shows several consistent trends within each profile and across each pit. Firstly, the present authors suggest that the $(Eu/Eu^*)/(Ce/Ce^*)$ ratio is lowest in the argillic horizon (Fig. 4)

because Ce^{4+} and Eu^{3+} adsorption is associated with Fe (oxyhydr)oxide, kaolinite, and interstratified clay surfaces. $(\text{Eu}/\text{Eu}^*)/(\text{Ce}/\text{Ce}^*)$ is largest in the saprolite because Eu^{2+} contained in primary minerals is oxidized ($\text{Eu}^{2+} \rightarrow \text{Eu}^{3+}$ in soil) and Ce^{3+} are adsorbed onto halloysite and/or smectite at depth. Some pits (R1C3 and R2P1) trend to lower $(\text{Eu}/\text{Eu}^*)/(\text{Ce}/\text{Ce}^*)$ values below 6 m, but as discussed, the depths to the saprolite-rock interface are unknown in this study. The A-horizon $(\text{Eu}/\text{Eu}^*)/(\text{Ce}/\text{Ce}^*)$ ratios trend to slightly larger values than the argillic horizons (Fig. 4), which can be attributed to low pH and organic-acid-rich conditions that would preferentially reduce, chelate, and mobilize Eu, while also affecting Ce^{3+} to a lesser extent. Although Laveuf and Cornu (2009) suggest the reduction of Eu is rare at the Earth's surface, the present authors do not discount that this is possible in the A-horizon at the site, particularly if catalyzed by the microbial community (Maleke et al., 2019).

Secondly, an overall trend of decreasing $(\text{Eu}/\text{Eu}^*)/(\text{Ce}/\text{Ce}^*)$ values with decreasing hillshed orders was observed (Fig. 4), which suggests a broad geomorphic effect on the degree of redox weathering. This hints that the landscape REEs are recording a long-term signal

that is, in part, related to interfluvial order. Within each pit, the paired lower elevation pits have a generally lower set of $(\text{Eu}/\text{Eu}^*)/(\text{Ce}/\text{Ce}^*)$ values, which again supports the notion that mobility and concentration of redox-sensitive REE respond to local landscape positions. No consistent trend was found in the land cover type (i.e. hardwood versus pine) versus the $(\text{Eu}/\text{Eu}^*)/(\text{Ce}/\text{Ce}^*)$ values and the data set is too limited to test the hypothesis that tree types are influencing these trends. Parallel studies of rooting density for these same pits suggested that cultivated, pine, and hardwood land use do influence carbon cycling dynamics (Billings & Sullivan, 2020), which probably would exert some control on redox, pH, and moisture conditions.

Isolating the different minerals using density and magnetic techniques could deepen understanding of the REE fractionation patterns. Minerals known to be REE hosts in the regional bedrock of the Cat Square and Charlotte terrains potentially include feldspars, hornblende, allanite, sphene, apatite, monazite, xenotime, and rhabdophane. Examining the extractable REE in the context of cation exchange properties would give further insights to understand pathways of migration. These possible mechanisms include: (1)

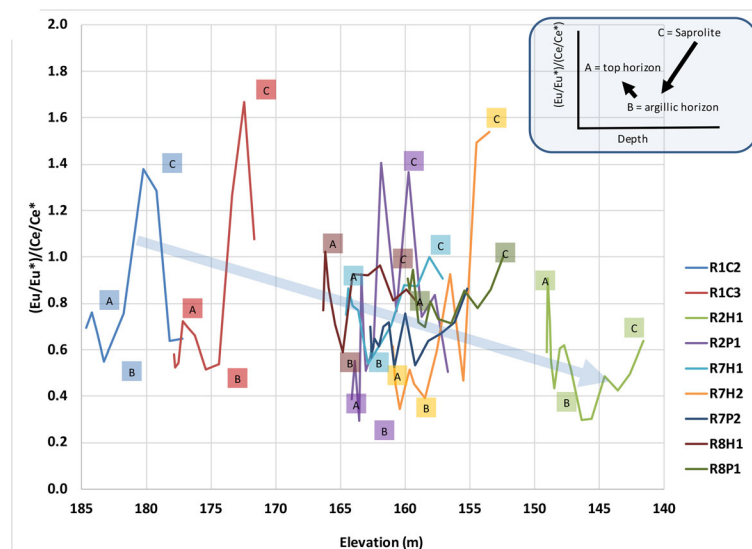


Fig. 4 Sample elevations versus europium anomaly (Eu/Eu^*) to cerium anomaly (Ce/Ce^*) ratio (see text for definition). Each profile is labeled by color. Colored square labels containing A, B, and C are the general locations of the A-horizon, argillic horizon, and saprolite horizon for the respectively colored lines. The large gray arrow symbolizes the general trend of decreasing $(\text{Eu}/\text{Eu}^*)/(\text{Ce}/\text{Ce}^*)$ with decreasing elevation (i.e. decreasing

interfluvial order). The upper right inset is a schematic representation common to each profile, where the ratio value is large in the saprolite, becomes lowest in the argillic horizon, and increases slightly in the A-horizon. See text for discussion regarding the relative mobility of Ce and Eu and their relation to parent rock composition

plant uptake, (2) erosion, (3) hydrolysis reactions with groundwater, (4) chelation, (5) leaching (Calabrese et al., 2018), (6) adsorption to clay minerals and (oxyhydr)oxides, and (7) precipitation as nanophases (Hochella et al., 2019).

Conclusions

The mineralogical and elemental analysis of material from regolith to a depth of 8 m in the Calhoun Critical Zone observatory revealed good agreement among independent methods of characterization, thus setting the stage for mass-balance assessments. Deep saprolites exhibit mineral assemblages and elemental compositions consistent with being derived from meta-granodioritic and Paleozoic meta-granitic to biotite/amphibolitic gneissic lithologies. Major saprolite minerals include ubiquitous quartz and kaolinite, with minor variable amounts of plagioclase, orthoclase, microcline, biotite, and phengite and with minor/trace variable amounts of vermiculite, smectite, hydrobiotite, goethite, gibbsite, halloysite, and hydroxy-interlayered-vermiculite (HIV). Argillic horizons (as defined herein by clay mineral abundance, i.e. not abundance of clay-sized particles) have the greatest amounts of kaolinite and interstratified kaolinite/smectite/vermiculite. A-horizons are quartz-rich and often contain minor HIV and allochthonous minerals, such as microcline. Aeolian transport is a likely mechanism for adding small amounts of mineral to the soils.

Argillic horizon thicknesses and their depths below the surface (as also defined by abundance Σ Al-Fe-H-oxides) and the CIA values for saprolites indicated that the architecture of weathering profiles is influenced by interfluvial order and landscape history. Higher-order interfluvial areas that are cultivated have thick argillic horizons that are depleted in alkali and alkali-earth cations (as indicated by tau plots) and are high in clay-mineral content. Intensely eroded landscape positions have thinner argillic horizons that are closer to the surface.

REE trends suggested that bedrock below the CCZO is variable in composition with affinities to meta-granodioritic and meta-granitic to biotite/amphibolitic gneiss. The sum of REE range from 30 to 1048 ppm with a general trend of highest values of sum REE associated with well-developed argillic horizons. Eu and Ce serve to proxy for

parent material and for redox sensitive conditions in the subsurface, respectively. The relative Eu and Ce anomaly ratios vary with both landscape position and location in the weathering profile. A general trend of larger Eu and Ce anomalies occurs at higher elevation (i.e. greater interfluvial order) and smaller anomalies in argillic horizons (relative to saprolite and A-horizons) regardless of landscape position.

The collective mineral and elemental composition of regolith throughout the CCZO is dependent upon a multigenerational (i.e. palimpsest) history of biogeochemical weathering acting upon the landscape over both human and geologic timescales. The data reported herein provide a basis to establish correlations in other critical zone research, such as studies of nutrient cycling (e.g. potassium uplift), geochronology (i.e. cosmogenic exposure ages and erosion rates), global carbon dynamics (CO₂ efflux versus soil respiration), the role of roots in soil structure, long-term geomorphic landscape evolution, and ecosystem services, that will allow for better discernment of landscape management and resource sustainability.

Supplementary Information The online version contains supplementary material available at <https://doi.org/10.1007/s42860-022-00202-8>.

Acknowledgments This work was supported by NSF grant EAR-GEO-1331846. Thanks are given to the entire team of Calzoners who can be recognized at <https://czo-archive.criticalzone.org/calhoun/people/>. The authors thank Will Cook for photographing the pits, data archiving, and management of the 2016 “Big Dig” program. USDA personnel assisted with the soil descriptions. Appreciation is also extended to Bruno Lanson, Marion Wampler, two anonymous reviewers, and editors who provided valuable feedback.

Authors Contributions All authors contributed equally to this effort, including field work, data analysis, and writing.

Funding This work was supported by NSF grant EAR-GEO-1331846.

Data Availability <https://czo-archive.criticalzone.org/national/>.

Declarations

Ethics Approval and Consent N/A

Consent for Publication N/A

Competing Interests The authors declare that they have no conflicts of interest.

References

- Anders, E., & Grevesse, N. (1989). Abundances of the elements: Meteoritic and solar. *Geochimica et Cosmochimica Acta*, *53*, 197–213.
- Austin, J. C., & Schroeder, P. A. (2014). Assessment of pedogenic gibbsite as a paleo-PCO₂ proxy using a modern Ultisol. *Clays and Clay Minerals*, *62*(5), 235–266.
- Austin, J. C., Richter, D. D., & Schroeder, P. A. (2020). Quantification of interstratified clays in multiple saturation states using NEWMOD2: Implications for the potassium uplift hypothesis in the SE United States. *Clays and Clay Minerals*, *68*(1), 67–80. <https://doi.org/10.1007/s42860-019-00060>
- Bacon, A.R. (2014) Pedogenesis and Anthropedogenesis on the southern Piedmont. Ph.D. Dissertation 3617449, Advisor, D.D. Richter, University program in Ecology Duke University. pp. 119.
- Bacon, A. R., Richter, D. D., Bierman, P. R., & Rood, D. H. (2012). Coupling meteoric ¹⁰Be with pedogenic losses of ⁹Be to improve soil residence time estimates on an ancient north American interfluve. *Geology*, *40*, 847–850. <https://doi.org/10.1130/G33449.1>
- Banwart, S., Menon, M., Bernasconi, S. M., Bloem, J., Blum, W. E. H., de Souza, D. M., Davidsdotir, B., et al. (2012). Soil processes and functions across an international network of critical zone observatories; Introduction to experimental methods and initial results. *Comptes Rendus Geoscience*, *344*(11–12), 758–772. <https://doi.org/10.1016/j.crte.2012.10.007>
- Bau, M. (1999). Scavenging of dissolved yttrium and rare earths by precipitating iron oxyhydroxide: Experimental evidence for Ce oxidation, Y-ho fractionation, and lanthanide tetrad effect. *Geochimica et Cosmochimica Acta*, *63*, 67–77.
- Bau, M., Koschinsky, A., Dulski, P., & Hein, J. R. (1996). Comparison of the partitioning behaviours of yttrium, rare earth elements, and titanium between hydrogenetic marine ferromanganese crusts and seawater. *Geochimica et Cosmochimica Acta*, *60*, 1709–1725.
- Bern, C. R., Yesavage, T., & Foley, N. K. (2017). Ion-adsorption REEs in regolith of the Liberty Hill pluton, South Carolina, USA: An effect of hydrothermal alteration. *Journal of Geochemical Exploration*, *172*, 29–33.
- Berner, R. A. (2004). *The Phanerozoic carbon cycle: CO₂ and O₂*. Oxford University Press.
- Billings, S. A., & Sullivan, P. L. (2020). Working across scales to project soil biogeochemical responses to climate. In Yang, Y., Keiluweit, M., Senesi, N., & Xing, B. (Eds.), *Multi-Scale Biogeochemical Processes in Soil Ecosystems: Critical Reactions and Resilience to Climate Changes* (pp. 1–12). Vol. 5 in IUPAC Series on Biophysico-Chemical Processes in Environmental Systems, John Wiley & Sons.
- Brantley, S. L., Lebedeva, M. I., Balashov, V. N., Singha, K., Sullivan, P. L., & Stinchcomb, G. (2017). Toward a conceptual model relating chemical reaction fronts to water flow paths in hills. *Geomorphology*, *277*, 100–117.
- Braun, J.-J., Pagel, M., Muller, J.-P., Bilong, P., Michard, A., & Guillet, B. (1990). Cerium anomalies in lateritic profiles. *Geochimica et Cosmochimica Acta*, *54*, 781–795.
- Brecheisen, Z. S., Cook, C. W., Heine, P. R., & Richter, D. D. (2019a). Micro-topographic roughness analysis (MTRA) highlights minimally eroded terrain in a landscape severely impacted by historic agriculture. *Remote Sensing of Environment*, *222*, 78–89.
- Brecheisen, Z. S., Cook, C. W., Heine, P. R., Ryang, J., & Richter, D. D. (2019b). Development and Deployment of a Field-Portable Soil O₂ and CO₂ Gas Analyzer and Sampler. *PLoS One*, *14*(8), e0220176. <https://doi.org/10.1371/journal.pone.0220176>
- Brecheisen, Z. S., Richter, D. D., Moon, S., & Halpin, P. N. (2021). Quantitative analysis of hillshed geomorphology and critical zone function: Raising the hillshed to watershed status. *GSA Bulletin*. <https://doi.org/10.1130/B35724.1>
- Brimhall, G. H., & Dietrich, W. E. (1987). Constitutive mass balance relations between chemical composition, volume, density, porosity, and strain in metasomatic hydrochemical systems: Results on weathering and pedogenesis. *Geochimica et Cosmochimica Acta*, *51*(3), 567–587.
- Calabrese, S., Richter, D. D., & Porporato, A. (2018). The formation of clay-enriched horizons by lessivage. *Geophysical Research Letters*, *45*(15), 7588–7595.
- Cannida, T. (2018) Petrography of the gneisses from the Mary Lou quarry, Clinton, SC: Implications for quantifying mineral compositions in the critical zone. University of Georgia, Athens, GA, USA. CURO Symposium. Program and Abstracts. p 58, <http://curo.uga.edu/symposium/BOAs/CURO2018BOA.pdf>
- Cecil, C. B. (2003). The concept of autocyclic and Allocyclic controls on sedimentation and stratigraphy, emphasizing the climatic variable. *Special Publication - Society for Sedimentary Geology*, *77*(October), 13–20.
- Chen, C., Barcellos, D., Richter, D. D., Schroeder, P. A., & Thompson, A. (2019). Redoximorphic Bt horizons of the Calhoun CZO soils exhibit depth-dependent iron-oxide crystallinity. *Journal of Soil Sedimentary*, *19*, 785–797.
- Churchman, G. J. (1990). Relevance of different intercalation tests for distinguishing halloysite from kaolinite in soils. *Clays and Clay Minerals*, *38*(6), 591–599.
- Cook, C.W. (2019). CCZO – photographic imagery, soil survey – soil pit profiles – Calhoun CZO – (2016–2016), HydroShare, <http://www.hydroshare.org/resource/ae1b338cc7a641f68fd5c4f85dba97a1>
- Coughlan, M. R., & Nelson, D. R. (2018). Influences of native American land use on the colonial euro-American settlement of the South Carolina Piedmont. *PLoS ONE*, *13*(3), e0195036.
- Coughlan, M. R., Nelson, D. R., Lonneman, M., & Block, A. E. (2017). Historical land use dynamics in the highly degraded landscape of the Calhoun critical zone observatory. *Land*, *6*(2), 32.
- Dennis, A. J., & Wright, J. E. (1997). The Carolina terrane in northwestern South Carolina, USA: Late Precambrian-Cambrian deformation and metamorphism in a peri-Gondwanan oceanic arc. *Tectonics*, *16*(3), 460–473.
- Dietel, J., Gröger-Trampe, J., Bertmer, M. S., Kaufhold, K. U., & Dohrmann, R. (2019). Crystal structure model development

- for soil clay minerals—I. Hydroxy-interlayered smectite (HIS) synthesized from bentonite. A multi-analytical study. *Geoderma*, 347, 135–149.
- Ferreira, E. P., Guerra, A. A. R., & de Azevedo, C. (2019). Rare earth elements in gneiss regoliths in southern Minas Gerais, Brazil. *Scientia Agricola*, 78(3). <https://doi.org/10.1590/1678-992X-2019-0190>
- Hack, J. T. (1975). Dynamic equilibrium and landscape evolution. *Theories of Landform Development*, 1, 87–102.
- Hauser, E., Richter, D. D., Markewitz, D., Brecheisen, Z., & Billings, S. A. (2020). Persistent anthropogenic legacies structure depth dependence of regenerating rooting systems and their functions. *Biogeochemistry*, 147, 259–275. <https://doi.org/10.1007/s10533-020-00641-2>
- Hochella Jr., M. F., Mogk, D., Ranville, J. I. A., Luther, G., Marr, L., McGrail, E. P., Murayama, M., Qafoku, N., Rosso, K., Sahai, N., Schroeder, P. A., Vikesland, P., Westerhoff, P., & Yang, Y. (2019). Natural, incidental, & engineered nanomaterials and their impacts on the earth system. *Science*. <https://doi.org/10.1126/science.aau8299>
- Holbrook, W. S., Marcon, V., Bacon, A. R., Brantley, S. L., Carr, B. J., Flinchum, B. A., Richter, D. D., & Riebe, C. S. (2019). Links between physical and chemical weathering inferred from a 65-m-deep borehole through Earth's critical zone. *Scientific Reports*, 9, 4495.
- Horkowitz, P. (1984). *Geology of the Philson crossroads 7.5' quadrangle, South Carolina - the nature of the boundary separating the inner Piedmont from the Carolina-Avalon terrane in central northwestern South Carolina* (M.S. thesis). University of South Carolina, 100p.
- Hu, Z., Haneklaus, S., Sparovek, G., & Schnug, E. (2006) Rare earth elements in soils. *Communications in Soil Science and Plant Analysis*, 37(9–10), 1381–1420.
- Huebner, M. T., Hatcher, R. D., & Merschat, A. J. (2017). Confirmation of the southwest continuation of the Cat Square terrane, southern Appalachian Inner Piedmont, with implications for middle Paleozoic collisional orogenesis. *American Journal of Science*, 317(2), 95–176.
- Hurst, V. J., Schroeder, P. A., & Styron, R. W. (1997). Accurate quantification of quartz and other phases by powder X-ray diffractometry. *Analytica Chimica Acta*, 337, 233–252.
- Jobbágy, G., & Jackson, B. (2004). The uplift of soil nutrients by plants: Biogeochemical consequences across scales. *Ecology*, 85(9), 2380–2389.
- Jordan, B. (2020) Geology of the Calhoun Critical Zone Observatory. M.S. Thesis, University of Georgia, Department of Geology, Athens, GA. 1 Map, 104 p. <https://exploro.libs.uga.edu/esploro/outputs/graduate/Geology-of-the-Calhoun-Critical-Zone-Observatory/9949348149502959>.
- Laveuf, C., & Comu, S. (2009). A review on the potentiality of rare earth elements to trace pedogenetic processes. *Geoderma*, 154, 1–12.
- Lebedeva, M. I., & Brantley, S. L. (2013). Exploring geochemical controls on weathering and erosion of convex hillslopes: Beyond the empirical regolith production function. *Earth Surface Processes and Landforms*, 38, 1793–1807.
- Li, L., Maher, K., Navarre-Sitchler, A., Druhan, J., Meile, C., Lawrence, C., Moore, J., Perdrial, J., Sullivan, P., & Thompson, A. (2017). Expanding the role of reactive transport models in critical zone processes. *Earth-Science Reviews*, 165, 280–301.
- Li, M. Y. H., & Zhou, M. F. (2020). The role of clay minerals in formation of regolith-hosted heavy rare earth element deposits. *American Mineralogist*, 105, 92–108.
- Maleke, M., Valverde, A., Gomez-Arias, A., Cason, E. D., Vermeulen, J. G., Coetsee-Hugo, L., Swart, H., van Heerden, E., & Castillo, J. (2019). Anaerobic reduction of europium by a clostridium strain as a strategy for rare earth biorecovery. *Scientific Reports*, 9(1), 14339. <https://doi.org/10.1038/s41598-019-50179-z>
- Markewich, H. W., & Markewich, W. (1994) *An overview of Pleistocene and Holocene inland dunes in Georgia and the Carolinas: Morphology, distribution, age, and paleoclimate*. U.S. Geological Survey bulletin: 2069.
- Moore, D. M., & Reynolds, R. C. (1997). *X-ray diffraction and the identification and analysis of clay minerals*. Oxford [England]. Oxford University Press.
- Moravec, B. G., Keifer, V., Root, R. A., White, A. M., Wang, Y., Olshansky, Y., McIntosh, J., & Chorover, J. (2021). Experimental weathering of a Volcaniclastic critical zone profile: Key role of colloidal constituents in aqueous geochemical response. *Chemical Geology*, 559. <https://doi.org/10.1016/j.chemgeo.2020.119886>
- Nesbitt, H., & Young, G. (1982). Early Proterozoic climates and plate motions inferred from major element chemistry of lutites. *Nature*, 299, 715–717. <https://doi.org/10.1038/299715a0>
- Price, J. R., & Velbel, M. A. (2003). Chemical weathering indices applied to weathering profiles developed on heterogeneous felsic metamorphic parent rocks. *Chemical Geology*, 202(3–4), 397–416.
- Raven, M. D., & Self, P. G. (2017). Outcomes of 12 years of the Reynolds cup quantitative mineral analysis round Robin. *Clays and Clay Minerals*, 65, 122–134. <https://doi.org/10.1346/CCMN.2017.064054>
- Richter, D. D., & Markewitz, D. (2001). *Understanding soil change: Soil sustainability over millennia, centuries, and decades*. Cambridge University Press.
- Richter, D. D., Eppes, M. C., Austin, J. C., Bacon, A. R., Billings, S. A., Brecheisen, Z., Ferguson, T. A., Markewitz, D., Pachon, J., Schroeder, P. A., & Wade, A. M. (2020). Soil production and the soil geomorphology legacy of grove Karl Gilbert. *Soil Science Society of America Journal*, 84(1), 1–20.
- Rietveld, H. (1967). Line profiles of neutron powder-diffraction peaks for structure refinement. *Acta Crystallogr.*, 22, 151.
- Ryland, R. C., Thompson, A., Sutter, L. A., & Markewitz, D. (2020). Mapping depth to the argillic horizon on historically farmed soil currently under forests. *Geoderma*, (369), 114291. <https://doi.org/10.1016/j.geoderma.2020.114291>
- Sanders, S.C. (2018) The fate of degraded biotites in the deep critical zone: Implications for the K-uplift hypothesis. University of Georgia Center for undergraduate research opportunities symposium. April 9-10, Athens, GA. Abstract with programs. p. 169 <http://curo.uga.edu/symposium/BOAs/CURO2018BOA.pdf>
- Schroeder, P. A. (2018). *Clays in the critical zone*. Cambridge University press (online ISBN: 9781316480083).
- Schroeder, P. A., Kim, J. G., & Melear, N. D. (1997). Mineralogical and textural criteria for recognizing remnant Cenozoic deposits on the Piedmont: Evidence from Sparta &

- Greene County, Georgia, U.S.A. *Sedimentary Geology*, 108, 195–206.
- Schroeder, P. A., Richter, D. D., & Sanders, S. C. (2020) The fate of degraded micas in the deep critical zone: Pathways to the formation of kaolinite and other secondary minerals in the S.E. US Piedmont. Geological Society of America meeting, northeastern/southeastern section, Reston, VA.
- St. Clair, J., Moon, S., Holbrook, W. S., Perron, J. T., Riebe, C. S., Martel, S. J., Carr, B., Harman, C., Singha, K., & Richter, D. D. (2019). Geophysical imaging reveals topographic stress control of bedrock weathering. *Science*, 350(6260), 534–538.
- Sullivan, P. L., Li, L., Godd ris, Y., & Brantley, S. L. (2020). Poised to Hindcast and Earthcast the effect of Climae on the critical zone: Shale Hills as a model. *Geophysical Monograph*, 250, 207–204.
- Thompson, A., Amistadi, M. K., Chadwick, O. A., & Chorover, J. (2013). Fractionation of yttrium and holmium during basaltic soil weathering. *Geochimica et Cosmochimica Acta*, 119, 18–30.
- Ufer, K., Roth, G., Kleeberg, R., Stanjek, H., Dohrmann, R., & Bergmann, J. (2004). Description of X-ray powder pattern of turbostratically disordered layer structures with a Rietveld compatible approach. *Zeitschrift f r Kristallographie*, 219, 519–527.
- Ufer, K., Stanjek, H., Roth, G., Dohrmann, R., Kleeberg, R., & Kaufhold, S. (2008). Quantitative phase analysis of bentonites by the Rietveld method. *Clays & Clay Minerals*, 56, 272–282.
- V zquez-Ortega, A., Perdrial, J., Harpold, A., Zapata-R os, X., Rasmussen, C., McIntosh, J., Schaap, M., Pelletier, J. D., Brooks, P. D., Amistadi, M. K., & Chorover, J. (2015). Rare earth elements as reactive tracers of biogeochemical weathering in forested rhyolitic terrain. *Chemical Geology*, 391, 19–32.
- Wymore, A., West, N., Maher, K., Sullivan, P., Harpold, A., Karwan, D., Marshall, J., Perdrial, J., Rempe, D., & Ma, L. (2017). Growing new generations of international critical zone scientists. *Earth Surface Processes and Landforms*. <https://doi.org/10.1002/esp.4196>

Springer Nature or its licensor holds exclusive rights to this article under a publishing agreement with the author(s) or other rightsholder(s); author self-archiving of the accepted manuscript version of this article is solely governed by the terms of such publishing agreement and applicable law.